INTERNATIONAL JOURNAL FOR NUMERICAL METHODS IN FLUIDS, VOL. 21, 901–931 (1995)

WAVELET AND MULTIPLE SCALE REPRODUCING KERNEL METHODS*

WING KAM LIU AND YIJUNG CHEN

Department of Mechanical Engineering, Northwestern University, 2145 Sheridan Road, Evanston, IL 60208, U.S.A.

SUMMARY

Multiple scale methods based on reproducing kernel and wavelet analysis are developed. These permit the response of a system to be separated into different scales. These scales can be either the wave numbers corresponding to spatial variables or the frequencies corresponding to temporal variables, and each scale response can be examined separately. This complete characterization of the unknown response is performed through the integral window transform, and a space–scale and time–frequency localization process is achieved by dilating the flexible multiple scale window function. An error estimation technique based on this decomposition algorithm is developed which is especially useful for local mesh refinement and convergence studies. This flexible space–scale window function can be constructed to resemble the well-known unstructured multigrid and *hp*-adaptive finite element methods. However, the multiple scale adaptive refinements are performed simply by inserting nodes into the highest wavelet scale solution region and at the same time narrowing the window function. Hence *hp*-like adaptive refinements can be performed without a mesh. An energy error ratio parameter is also introduced as a measure of aliasing error, and critical dilation parameters are determined for a class of spline window functions to obtain optimal accuracy. This optimal dilation parameter dictates the number of nodes covered under the support of a given window function. Numerical examples, which include the Helmholtz equation and the 1D and 2D advection–diffusion equations, are presented to illustrate the high accuracy of the methods using the optimal dilation parameter, the concept of multiresolution analysis and the meshless unstructured adaptive refinements.

KEY WORDS: wavelet; multiple scale methods; optimal dilation parameter

1. INTRODUCTION

Owing to geometry, boundary conditions, body forces and strong advection, high gradients and mixed mode (high, medium and low frequencies) response are often encountered during the solution of complex physical problems. Exact solutions are usually not available. Numerical solutions based on the traditional finite element method (FEM) require a fine mesh, and local mesh refinement may not be reliable when the exact solution is unknown. In order to overcome this difficulty, multiple scale analysis by reproducing kernel and wavelet particle methods is established.

Multiple scale analysis has its origin in signal analysis. Wavelet analysis is a contemporary science in image processing, but one major drawback in its application to computational mechanics is its incapability of handling complex boundary conditions. Reproducing kernel particle methods (RKPMs), proposed by Liu *et al.*,[1–4] have the ability to adjust to different boundary conditions with a boundary correction term. Adopting this advantage of RKPMs, new multiple scale analysis methods which can handle arbitrary geometry are developed in this paper.

* This is an extended version of a paper presented at the 2nd Japan–U.S. Symposium on Finite Element Methods in Large-Scale Computational Fluid Dynamics, Tokyo, 14–16 March 1994.

CCC 0271–2091/95/100901–31

Received 30 May 1994
Revised 27 September 1994

For computational mechanics, system discretization is inevitable. When a system is discretized, aliasing is introduced into the response. If the response of the system is band-limited, which means that the response is non-zero only in a certain interval of its Fourier transform domain, a solution free of aliasing error is readily calculated. However, for a complex system, aliasing may interact with the high frequency part of the response and it becomes impossible to separate them clearly. In these cases, reducing the effect of aliasing is a major step to improving the solution.

However, aliasing is not without its redeeming features for multiple scale analysis. Since aliasing is a byproduct of undersampling, its portion in the total solution is a good index of error estimation. Furthermore, the multiple scale RKPM has a built-in time–frequency or space–wave number localization ability. From this advantage of the multiple scale RKPM, local aliasing estimation can easily be determined. Furthermore, using this local aliasing information, local refinement or *hp*-like adaptive refinement without a mesh can be carried out without the help of the exact solution.

In the next section, the multiple scale wavelet particle method is developed. In Section 3 the multiple scale reproducing kernel particle method is derived. In Section 4 a window dilation parameter and a simple convergence parameter are introduced to control the accuracy and convergence of solution. The analogy between the multiple scale RKPM and the *hp*-adaptive finite element method is also discussed. Examples of multiple scale decomposition and meshless unstructured adaptive refinements using the highest wavelet scale solutions are presented in Section 5. Conclusions are given in Section 6.

2. DEVELOPMENT OF MULTIPLE SCALE WAVELET PARTICLE METHODS (WPMS)

2.1. *Review of multiresolution analysis*[5,6]

The framework of a multiresolution analysis consists of a sequence of nested closed subspaces

$$\{0\} = V_\infty \subset \cdots \subset V_1 \subset V_0 \subset V_{-1} \subset \cdots \subset V_{-\infty} = L^2(R).$$

The basis functions which generate these subspaces are scaling functions. Scaling functions are a family of functions which are generated by the translation (n) and dilation (m) of a single function $\phi(x)$. This family of functions, denoted by $\phi_{mn}(x)$, is given by

$$\phi_{mn}(x) = 2^{-m/2}\phi\left(\frac{x}{2^m} - n\right), \quad m, n \in \mathscr{Z} = [\ldots, -1, 0, 1, \ldots], \tag{1a}$$

or in normalized form (with respect to the mesh parameter Δx) by

$$\phi_{mn}\left(\frac{x}{\Delta x}\right) = 2^{-m/2}\phi\left(\frac{x}{2^m \Delta x} - n\right), \quad m, n \in \mathscr{Z}. \tag{1b}$$

An illustration of the translation and dilation for a given window function is presented in Figure 1. As can be seen in subsequent development, through the implementation of this type of window function and the exploitation of the Fourier transform it is possible to develop a new type of shape function that is closely related to finite elements, and these new shape functions can still be used in the usual Galerkin formulation. The derivative of the shape function, and thus reproducing kernel, can be obtained by direct differentiation without a finite element mapping. The two parameters in the scaling function provide the ability to translate and dilate the window function. Translation is required to move the window function around the domain, since the window functions themselves have a compact support. *The ability to translate replaces the need to define elements. The dilation parameter is used to provide refinement.* This dilation parameter also controls the convergence rate of the multiple scale RKPM. As shown in the numerical examples,[1] the rate of convergence of the L_2-norm (H_1-norm) of a

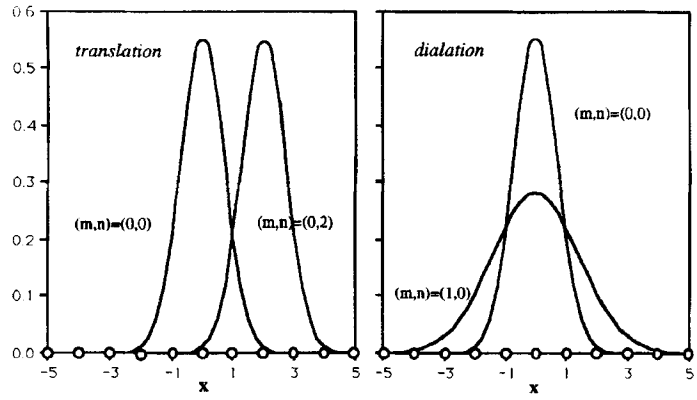

Figure 1. Examples of translation (n) and dilation (m)

smooth Laplacian solution varies from 2 to 16 (from 1 to 15) for a Gaussian window and from 2 to 5 (from 1 to 4) for a cubic spline window by simply changing the *refinement* or dilation parameter of a single window function. This combination of translation and dilation produces a *meshless p-like adaptive variable node multiple scale RKPM.* The larger the dilation parameter, the smaller the frequency band is in the solution and the larger the critical time step becomes in dynamic analyses.[3] The refinement parameter transformation between the time and frequency domain (or space and wave number) controls the solution space. This introduces the ability to choose the size of the frequency or wave number range in the calculation.

The complementary subspace W_m of V_m is defined by

$$V_{m-1} = V_m + W_m. \tag{2}$$

A *wavelet*, which is a function that generates the spaces W_m, $m \in \mathscr{Z}$, in the same manner as a scaling function $\phi(x)$ generates the spaces V_m, $m \in \mathscr{Z}$, is defined by

$$W_m = \{\psi_{mn}, n \in \mathscr{Z}\}. \tag{3}$$

This family of functions, denoted by $\psi_{mn}(x)$, is given by

$$\psi_{mn}(x) = 2^{-m/2}\psi\left(\frac{x}{2^m} - n\right), \quad m, n \in \mathscr{Z}, \tag{4a}$$

or in normalized form (with respect to the mesh parameter Δx) by

$$\psi_{mn}\left(\frac{x}{\Delta x}\right) = 2^{-m/2}\psi\left(\frac{x}{2^m \Delta x} - n\right), \quad m, n \in \mathscr{Z}. \tag{4b}$$

From (2) this family of subspaces of $L^2(R)$ gives a direct sum decomposition of $L^2(R)$ such that

$$L^2(R) = \cdots + (V_{-2} - V_{-1}) + (V_{-1} - V_0) + (V_0 - V_1) + \cdots = \cdots + W_{-1} + W_0 + W_1 + \cdots. \tag{5}$$

A wavelet ψ in $L^2(R)$ is called an orthogonal wavelet if $\{\psi_{mn}\}$ satisfies

$$\langle \psi_{mn}, \psi_{kl} \rangle = \delta_{mk}\, \delta_{nl}, \tag{6}$$

where $\langle \cdot \rangle$ is the inner product operator and δ_{mk} is the Kronecker delta.

If ψ is an orthogonal wavelet, then the direct sum in (5) becomes an orthogonal sum

$$L^2(R) = \cdots \oplus W_{-1} \oplus W_0 \oplus W_1 + \cdots. \tag{7}$$

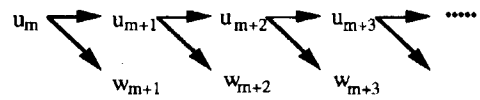

Figure 2. Multiresolution decomposition algorithm

For any given function $u \in L^2(R)$ there exists a unique decomposition

$$u = \cdots + w_{-1} + w_0 + w_1 + \cdots, \tag{8a}$$

where $w_m \in W_m$. The level m resolution of the given function u is represented by

$$u \approx u_m = w_{m+1} + w_{m+2} + \cdots. \tag{8b}$$

Since $V_m = V_{m+1} + W_{m+1}$ for any $m \in \mathscr{Z}$, u_m has a unique decomposition

$$u_m = u_{m+1} + w_{m+1}, \tag{9}$$

where $u_{m+1} \in V_{m+1}$ and $w_{m+1} \in W_{m+1}$. By repeating this process, we have a decomposition algorithm from the finest scale to the coarser ones as depicted in Figure 2.

For a simple illustration and a comparison with linear finite elements, linear orthogonal scaling functions and wavelets are discussed in this paper. The equations for linear scaling functions and wavelets are given in Appendix I. For orthogonal scaling functions and wavelets the reconstruction formula is given by

$$u = \sum_{m,n \in \mathscr{Z}} \langle u, \psi_{mn} \rangle \psi_{mn}(x); \tag{10a}$$

for the level M resolution of given function u the reconstruction formula is given by

$$u_M = \sum_{n \in \mathscr{Z}} \langle u, \phi_{Mn} \rangle \phi_{Mn}(x) = \sum_{m=M}^{\infty} \sum_{n \in \mathscr{Z}} \langle u, \psi_{mn} \rangle \psi_{mn}(x). \tag{10b}$$

2.2. *Multiple scale wavelet particle method*

Particle forms of wavelet analysis can be achieved by breaking down the inner product terms of (10) into subinterval integration ($B^m(n)$) and assuming that the response $u(x)$ is constant in each of the subintervals, i.e.

$$\langle u, \phi_{mn} \rangle = \sum_{i}^{x_i \in B^m(n)} \left(\int_{B^m(n)} \phi_{mn}(x)\, \mathrm{d}x \right) u_i, \tag{11a}$$

$$\langle u, \psi_{mn} \rangle = \sum_{i}^{x_i \in B^m(n)} \left(\int_{B^m(n)} \psi_{mn}(x)\, \mathrm{d}x \right) u_i, \tag{11b}$$

or, using a numerical quadrature integration scheme,

$$\langle u, \phi_{mn} \rangle = \sum_{i}^{x_i \in B^m(n)} \phi_{mn}(x_i) \Delta V_i u_i, \tag{11c}$$

$$\langle u, \psi_{mn} \rangle = \sum_{i}^{x_i \in B^m(n)} \psi_{mn}(x_i) \Delta V_i u_i, \tag{11d}$$

where $B^m(n)$ is the support of the mth scale window function at translation position n and ΔV_i is the ith nodal volume evaluated at x_i. Substituting (11) into (10) and applying the decomposition algorithm given in Section 2.1, we obtain our desired discrete multiresolution of $u(x)$ as

$$u(x) \approx u_m(x) = w_{m+1}(x) + w_{m+2}(x) + w_{m+3}(x) + \cdots, \tag{12}$$

where

$$u_m(x) = \sum_{i=1}^{NP} N_i^m(x) u_i, \tag{13a}$$

$$w_m(x) = \sum_{i=1}^{NP} \bar{N}_i^m(x) u_i, \tag{13b}$$

with

$$N_i^m(x) = \sum_{n=n_1}^{n_2} \left(\int_{B^m(n)} \phi_{mn}(x)\, \mathrm{d}x \right) \phi_{mn}(x), \quad x_i \in B^m(n), \tag{14a}$$

$$\bar{N}_i^m(x) = \sum_{n=n_1}^{n_2} \left(\int_{B^m(n)} \psi_{mn}(x)\, \mathrm{d}x \right) \psi_{mn}(x), \quad x_i \in B^m(n), \tag{14b}$$

or, using a quadrature formula to discretize the integrals,

$$N_i^m(x) = \sum_{n=n_1}^{n_2} \left[\phi_{mn}(x_i) \Delta V_i \right] \phi_{mn}(x), \quad x_i \in B^m(n), \tag{14c}$$

$$\bar{N}_i^m(x) = \sum_{n=n_1}^{n_2} \left[\psi_{mn}(x_i) \Delta V_i \right] \psi_{mn}(x), \quad x_i \in B^m(n). \tag{14d}$$

Here NP is the total number of points used in the particle method and n_1 and n_2 are the left and right limits of wavelet translation numbers respectively. The boundary correction for a finite domain problem in this wavelet particle method is achieved by applying the mirror-image outside the domain. A review of the mirror-image boundary correction technique is given in Appendix II. For most cases the best result is obtained by choosing $m = 0$ in the normalized form (1b). After the finest scale result has been derived, all other coarser scale results can be obtained automatically by the decomposition algorithm.

2.3. Reproducing kernel and wavelet particle method

An intrinsic property of polynomial-based wavelets is the requirement that

$$\int x^m \psi(x) \mathrm{d}x = 0, \quad m = 0, 1, \ldots, q, \tag{15}$$

where q is the degree of the polynomial of the mother wavelet $\psi(x)$. From (15) it follows that a qth-order wavelet cannot represent the $1, x, x^2, \ldots, x^q$ parts of the solution. To remedy this deficiency, we shall represent a function $u(x)$ by

$$u(x) = u^{\mathrm{w}}(x) + \mathbf{P}(x)\mathbf{c}, \tag{16}$$

where $u^{\mathrm{w}}(x)$ is the part of the solution that is obtained by the multiresolution wavelet reconstruction as given in Section 2.2. $\mathbf{P}(x) = \{P_1(x), P_2(x), \ldots, P_n(x)\}$ and $\mathbf{c} = \{c_1, c_2, \ldots, c_n\}^{\mathrm{T}}$ are the vectors of the n linearly independent functions and unknown coefficients respectively. Superscript T denotes the

transpose. We can consider the term $\mathbf{P}(x)\mathbf{c}$ as the residual representation of $u(x)$ within a bounded domain. If $[P_1(x), P_2(x)]$ is chosen to be $[1, x]$, then $u(x)$ can be given as

$$u(x) = u^{\mathrm{w}}(x) + [1, x]\begin{bmatrix} c_1 \\ c_2 \end{bmatrix}. \tag{17}$$

The constants c_1 and c_2 can be derived by premultiplying both sides by $\mathbf{P}^{\mathrm{T}}$ and a local window function $\phi((x-y)/a_0)$ centred at the point of interest x and integrating over the whole domain V:

$$\int_v \begin{bmatrix} 1 \\ y \end{bmatrix} \phi\left(\frac{x-y}{a_0}\right) u(y)\, \mathrm{d}y = \int_v \begin{bmatrix} 1 \\ y \end{bmatrix} \phi\left(\frac{x-y}{a_0}\right) \left(u^{\mathrm{w}}(y) + [1 \;\; y]\begin{bmatrix} c_1 \\ c_2 \end{bmatrix}\right) \mathrm{d}y. \tag{18}$$

It is noted that a_0 is the dilation parameter. Rearranging terms in (18), we get

$$\int_v \begin{bmatrix} 1 \\ y \end{bmatrix} \phi\left(\frac{x-y}{a_0}\right) u(y)\, \mathrm{d}y = \int_v \begin{bmatrix} 1 \\ y \end{bmatrix} \phi\left(\frac{x-y}{a_0}\right) u^{\mathrm{w}}(y)\, \mathrm{d}y + \int_v \begin{bmatrix} 1 & y \\ y & y^2 \end{bmatrix} \phi\left(\frac{x-y}{a_0}\right) \mathrm{d}y \begin{bmatrix} c_1 \\ c_2 \end{bmatrix}. \tag{19}$$

Define a 2×2 matrix $\mathbf{M}(x)$ as

$$\mathbf{M}(x) = \int_v \begin{bmatrix} 1 & y \\ y & y^2 \end{bmatrix} \phi\left(\frac{x-y}{a_0}\right) \mathrm{d}y = \begin{bmatrix} \displaystyle\int_v \phi\left(\frac{x-y}{a_0}\right) \mathrm{d}y & \displaystyle\int_v y\phi\left(\frac{x-y}{a_0}\right) \mathrm{d}y \\ \displaystyle\int_v y\phi\left(\frac{x-y}{a_0}\right) \mathrm{d}y & \displaystyle\int_v y^2\phi\left(\frac{x-y}{a_0}\right) \mathrm{d}y \end{bmatrix}. \tag{20}$$

Then the constants c_1 and c_2 can be shown to be

$$\begin{bmatrix} c_1 \\ c_2 \end{bmatrix} = \mathbf{M}^{-1}\left[\int_v \begin{bmatrix} 1 \\ y \end{bmatrix} u(y)\phi\left(\frac{x-y}{a_0}\right) \mathrm{d}y - \int_v \begin{bmatrix} 1 \\ y \end{bmatrix} u^{\mathrm{w}}(y)\phi\left(\frac{x-y}{a_0}\right) \mathrm{d}y\right]. \tag{21}$$

Substituting (21) into (17), we have

$$\begin{aligned} u(x) &= u^{\mathrm{w}} + [1 \;\; x]\mathbf{M}^{-1}\left[\int_v \begin{bmatrix} 1 \\ y \end{bmatrix} u(y)\phi\left(\frac{x-y}{a_0}\right) \mathrm{d}y - \int_v \begin{bmatrix} 1 \\ y \end{bmatrix} u^{\mathrm{w}}(y)\phi\left(\frac{x-y}{a_0}\right) \mathrm{d}y\right] \\ &= u^{\mathrm{w}}(x) + \int_v [1 \;\; x]\mathbf{M}^{-1}\begin{bmatrix} 1 \\ y \end{bmatrix} u(y)\phi\left(\frac{x-y}{a_0}\right) \mathrm{d}y \\ &\quad - \int_v [1 \;\; x]\mathbf{M}^{-1}\begin{bmatrix} 1 \\ y \end{bmatrix} u^{\mathrm{w}}(y)\phi\left(\frac{x-y}{a_0}\right) \mathrm{d}y. \end{aligned} \tag{22}$$

Following the procedure described by Liu *et al.*,[1-4] the term $[1 \;\; x]\mathbf{M}^{-1}[1 \;\; y]^{\mathrm{T}}$ can be expressed in terms of the moments of the window function, i.e.

$$[1 \;\; x]\,\mathbf{M}^{-1}\begin{bmatrix} 1 \\ y \end{bmatrix} = c_1(x) + c_2(x)\left(\frac{x-y}{a_0}\right), \tag{23a}$$

and a correction function $C(x, y, a_0)$ is defined as

$$C(x, y, a_0) = c_1(x) + c_2(x)\left(\frac{x-y}{a_0}\right), \tag{23b}$$

where

$$c_1(x) = -\frac{1}{a_0}\frac{m_{11}(x)}{m_0(x)m_{11}(x) - m_1^2(x)}, \tag{24a}$$

$$c_2(x) = \frac{1}{a_0} \frac{m_1(x)}{m_0(x)m_{11}(x) - m_1^2(x)}. \tag{24b}$$

The moments m_0, m_1 and m_{11} are defined as

$$m_0(x) = \int_v \phi\left(\frac{x-y}{a_0}\right) \mathrm{d}y, \tag{25a}$$

$$m_1(x) = \int_v y\phi\left(\frac{x-y}{a_0}\right) \mathrm{d}y, \tag{25b}$$

$$m_{11}(x) = \int_v y^2\phi\left(\frac{x-y}{a_0}\right) \mathrm{d}y. \tag{25c}$$

Equation (17) can be written in the more general form

$$u(x) = u^{\mathrm{w}}(x) + \int_v C(x, y, a_0)\phi\left(\frac{x-y}{a_0}\right)u(y)\,\mathrm{d}y - \int_v C(x, y, a_0)\phi\left(\frac{x-y}{a_0}\right)u^{\mathrm{w}}(y)\,\mathrm{d}y. \tag{26}$$

It is noted that the second term in (26) is the reproducing kernel approximation presented by Liu *et al.*[1-4] The first term is the multiresolution wavelet part, whereas the third term couples the two methods. It is interesting to point out that by a proper choice of a_0, the contribution of the coupling term can be shown to be negligible. With this construction the wavelet and reproducing kernel terms give the high and low frequency (or the fine and coarse scale) representations of the solution u respectively. It is also noted that $u^{\mathrm{w}}(x)$ can be expressed by other continuous or discrete multiple scale reproducing kernels. Via this decomposition, adaptive refinements by simply inserting nodes in the unresolved high frequency/wave number (or fine scale) region can be developed, but without a mesh.

To further examine this multiple frequency/wave number band wavelet approximation, we let

$$u^{\mathrm{w}}(x) = \sum_{m=0}^{\infty} \sum_{n=n_1}^{n_2} \langle u, \psi_{mn}\rangle \psi_{mn}(x). \tag{27}$$

Substituting (27) into (26) yields

$$u(x) = \int_v C(x, y, a_0)\phi\left(\frac{x-y}{a_0}\right)u(y)\,\mathrm{d}y + \sum_{m=0}^{\infty} \sum_{n=n_1}^{n_2} \left(\int_v u(y)\psi_{mn}(y)\,\mathrm{d}y\right)\left[\psi_{mn}(x) - \tilde{\psi}_{mn}(x)\right]. \tag{28}$$

The approximation of the wavelet functions $\psi_{mn}(x)$ through the reproducing kernel, denoted by $\tilde{\psi}_{mn}(x)$, is

$$\tilde{\psi}_{mn}(x) = \int_v C(x, y, a_0)\phi\left(\frac{x-y}{a_0}\right)\psi_{mn}(y)\,\mathrm{d}y. \tag{29}$$

It is now clear from (29) that $\tilde{\psi}_{mn}(x)$ is simply an approximation of $\psi_{mn}(x)$ via the reproducing kernel reconstruction. It is expected that $\tilde{\psi}_{mn}(x)$ is very close to $\psi_{mn}(x)$ for low frequency/wave number wavelets. Consequently, the contribution from the low frequency/wave number wavelets is close to zero. Depending on the choice of a_0, ϕ and ψ, the reproducing kernel might not be able to reconstruct the high frequency/wave number part of the solution (first term in (28)). These high frequency/wave number components can be readily picked up by multiresolution wavelet analysis.

3. MULTIPLE SCALE REPRODUCING KERNEL PARTICLE METHOD (RKPM)

The reproducing kernel particle method developed by Liu *et al.*[1-4] is given by

$$u^R(x) = \int_\Omega C(a_0, x, y)\phi\left(\frac{x-y}{a_0}\right)u(y)\,dy \tag{30a}$$

or its discrete form

$$u^h(x) = \sum_{i=1}^{NP}\left[C(a_0, x, x_i)\phi\left(\frac{x-x_i}{a_0}\right)\Delta x_i\right]u(x_i). \tag{30b}$$

With the help of the boundary correction term $C(a_0, x, x_i)$, the reproducing of a given function can be treated as a finite convolution of the given function and the kernel function $\phi(x/a_0)$. From the Fourier transform study we note that this kernel function serves as a lowpass filter in the reconstruction procedure. The multiple scale RKPM is defined by a family of kernel functions $\phi_m(x)$ given by

$$\phi_0(x) = \phi\left(\frac{x}{a_0}\right), \tag{31a}$$

$$\phi_m(x) = \phi\left(\frac{x}{2^m a_0}\right). \tag{31b}$$

Their Fourier transform relationship is given by

$$\hat{\phi}_m(\xi) = \hat{\phi}_0(2^m\xi). \tag{31c}$$

The wavelets corresponding to these kernel functions are defined by

$$\psi_{m+1}(x) = \phi_m(x) - \phi_{m+1}(x). \tag{32a}$$

The Fourier transform of (32a) implies

$$\hat{\psi}_{m+1}(\xi) = \hat{\phi}_m(\xi) - \hat{\phi}_{m+1}(\xi). \tag{32b}$$

An example using a Gaussian function as the kernel function is illustrated in Figure 3.

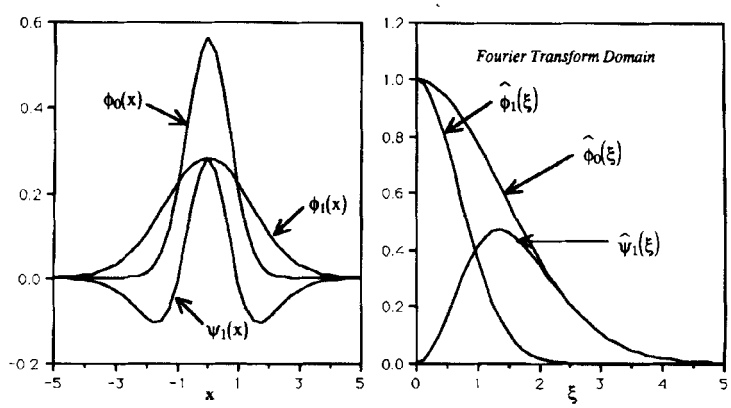

Figure 3. Kernel function and corresponding wavelet function

By substituting (32a) into (30a) and repeating it for as many levels as we need, a multiple scale decomposition of a given response is obtained as

$$\begin{aligned} u^{\mathrm{h}}(x) &= u_0(x) && \text{(finest scale)} \\ &= w_1(x) + u_1(x) && \text{(two-level decomposition)} \\ &= w_1(x) + w_2(x) + u_2(x) && \text{(three-level decomposition)} \\ &= \cdots && \text{(up to arbitrary levels),} \end{aligned} \tag{33}$$

where

$$u_m(x) = \int_v C(2^m a_0, x, y)\phi_m(x-y)u(y)\,\mathrm{d}y, \tag{34a}$$

$$w_m(x) = \int_v \psi_m(x-y)u(y)\,\mathrm{d}y, \tag{34b}$$

with

$$\psi_m(x-y) = C(2^{m-1}a_0, x, y)\phi_{m-1}(x-y) - C(2^m a_0, x, y)\phi_m(x-y). \tag{34c}$$

Similarly to the multiple scale wavelet particle method, the multiple scale RKPM always starts from the finest scale and the various levels of the response can be derived by the decomposition algorithm.

Remark

As proposed by Liu *et al.*,[1-4] with the boundary correction term the shape function of the RKPM satisfies the consistency condition but does not satisfy the Kronecker delta property. To satisfy the Kronecker delta property, let

$$u^{\mathrm{h}}(x_i) = \sum_{j=1}^{NP} N_j(x_i)u_j \equiv \sum_{j=1}^{NP} A_{ij}u_j, \tag{35}$$

where $A_{ij} = N_j(x_i)$; then

$$u_j = A_{ij}^{-1}u_i^{\mathrm{h}}, \qquad u_i^{\mathrm{h}} = u^{\mathrm{h}}(x_i). \tag{36}$$

With the help of this linear transformation we have

$$u^{\mathrm{h}}(x) = \sum_{i=1}^{np}\left(\sum_{j=1}^{np} A_{ij}^{-1}N_j(x)\right)u_i^{\mathrm{h}} = \sum_{i=1}^{np}\tilde{N}_i(x)u_i^{\mathrm{h}}. \tag{37}$$

This new shape function $\tilde{N}_i(x)$ will satisfy the Kronecker delta property. However, from numerical experiments the accuracy of the solution and its convergence rate are mainly effected by the chosen dilation parameter, which will be discussed in the next section. Because the new shape function $\tilde{N}_i(x)$ is based on a linear transformation of the shape function $N_i(x)$, both shape functions give identical accuracy and convergence rate.

4. CHOOSING THE OPTIMAL DILATION PARAMETER a_0

4.1. An energy approach

A practical approach for choosing the dilation parameter a_0 for the reproducing kernel window is to determine the interaction between the size of the given window and the sampling rate of the given nodal system in the Fourier transform domain. The Fourier transform of the reproducing kernel

window function $\phi(x)$ is also a window $\hat{\phi}(\xi)$ in the transform domain. The definitions of the centre ξ^* and radius $\Delta\hat{\phi}$ of a window function $\hat{\phi}(\xi)$ are given by[5]

$$\xi^* = \frac{1}{\|\hat{\phi}\|_2^2} \int_{-\infty}^{\infty} \xi |\hat{\phi}(\xi)|^2 \, d\xi, \tag{38}$$

$$\Delta\hat{\phi} = \frac{1}{\|\hat{\phi}\|_2} \left(\int_{-\infty}^{\infty} (\xi - \xi^*) |\hat{\phi}(\xi)|^2 \, d\xi \right). \tag{39}$$

The width of the window function is defined by $2\Delta\hat{\phi}(\xi)$. The norm of $\hat{\phi}(\xi)$ is defined as

$$\|\hat{\phi}\|_2 = \left(\int_{-\infty}^{\infty} \hat{\phi}(\xi) \overline{\hat{\phi}(\xi)} \, d\xi \right)^{1/2}. \tag{40}$$

The ratio of the area located inside the sampling rate region to the whole area under the window $\hat{\phi}(\xi)$ is defined as

$$\frac{dE}{E} = \frac{\|\hat{\phi} - \hat{\phi}_N\|_2^2}{\|\hat{\phi}\|_2^2}, \tag{41}$$

where $\hat{\phi}_N(\xi)$ is the window area located in a given interval $[-\xi_N, \xi_N]$ and $\xi_N = \pi/\Delta x$ (sampling rate). In signal analysis this is the energy error ratio in the reconstruction procedure.[7]

For a Gaussian window

$$\phi\left(\frac{x}{a_0}\right) = \frac{1}{a_0\sqrt{\pi}} \exp\left[-\left(\frac{x}{a_0}\right)^2 \right], \tag{42a}$$

$$a_0\hat{\phi}(a_0\xi) = \exp\left[-\left(\frac{a_0\xi}{2}\right)^2 \right]. \tag{42b}$$

The energy error ratio is given as

$$\frac{dE}{E} = 1 - \operatorname{erf}\left(\frac{a_0\pi}{\sqrt{2}\Delta x} \right), \tag{43}$$

where a_0 is the dilation parameter of the window and erf(.) is the error function. The error function is defined as

$$\operatorname{erf}(x) = \frac{2}{\sqrt{\pi}} \int_0^x e^{-y} \, dy. \tag{44}$$

The relationship between dE/E and $a_0\pi/\sqrt{2}\Delta x$ at the specific values used in this paper is given in Table I (a bold number denotes an optimal parameter).

Table I. Gaussian function

dE/E (%)	$a_0\pi/\sqrt{2}\Delta x$	dE/E (%)	$a_0\pi/\sqrt{2}\Delta x$
0·001	3·123413275	1	1·821386383
0·01	**2·751063909**	8	1·237922073
0·1	2·326753771	20	0·9061938125

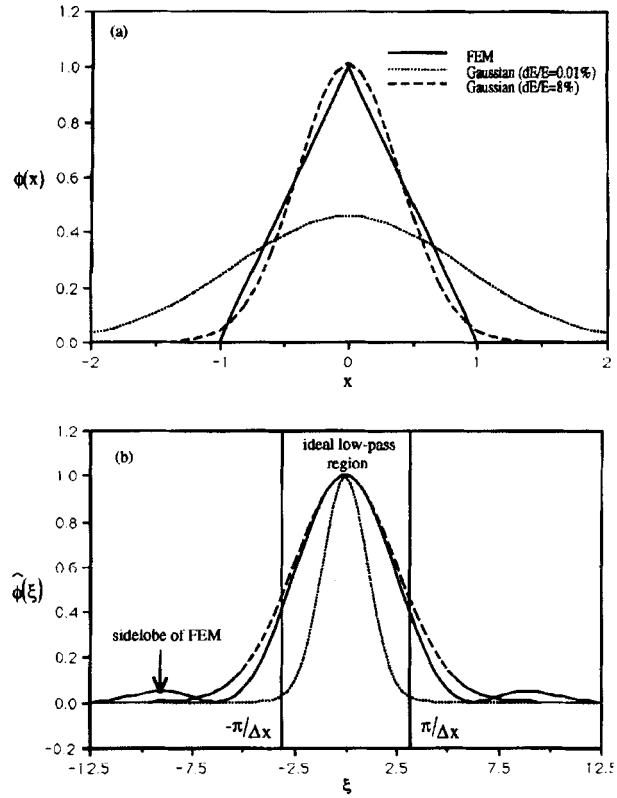

Figure 4. (a) Three window functions: FEM, Gaussian with $dE/E = 0{\cdot}01\%$ and Gaussian with $dE/E = 8\%$. (b) Their Fourier transforms

A large window (in the function domain) filters out the fine scales (small wave numbers or high frequencies) which are caused by sampling aliasing; consequently, oscillation in the solution may occur. In contrast, a small window (in the function domain) may introduce aliasing but will cover wider scale/frequency bands. From the definition of the energy error ratio the linear finite element shape function, which is a compactly supported triangular window, may cause approximately 8% energy error. For a Gaussian window, from experience, $dE/E = 0{\cdot}01\%$ will give very good solutions and can minimize oscillatory solutions. Figure 4 shows the shapes of the linear FEM, Gaussian with $dE/E = 8\%$ and Gaussian with $dE/E = 0{\cdot}01\%$ windows in the function and Fourier transform domains. The Gaussian window with $dE/E = 8\%$ has a shape similar to that of the linear FEM window in both the function and Fourier transform domains. It is clear that the FEM window is compactly supported in the space domain but the Gaussian window has infinite support; the Gaussian window decays rapidly outside the ideal lowpass filter region in the transform domain but the FEM window has a side-lobe towards infinity (see Figure 4). In general these two windows show similar performance in terms of absolute accuracy and convergence rate, but for a band-limited solution, which is non-zero in a certain range in the transform domain and zero outside the limit, the Gaussian window will give more accurate results. This is because the side-lobe of the FEM window will introduce aliasing in the reconstruction procedure. This will be illustrated via a Helmholtz equation in Section 5.1. Similar frequency studies of the spline family are presented in Figure 5 and Table II (a bold number denotes an optimal parameter). The detailed analysis of the spline family (from box function to cubic spline) is given in Appendix III. As can be seen from Figure 5(b), the side-lobes of the spline family in the frequency

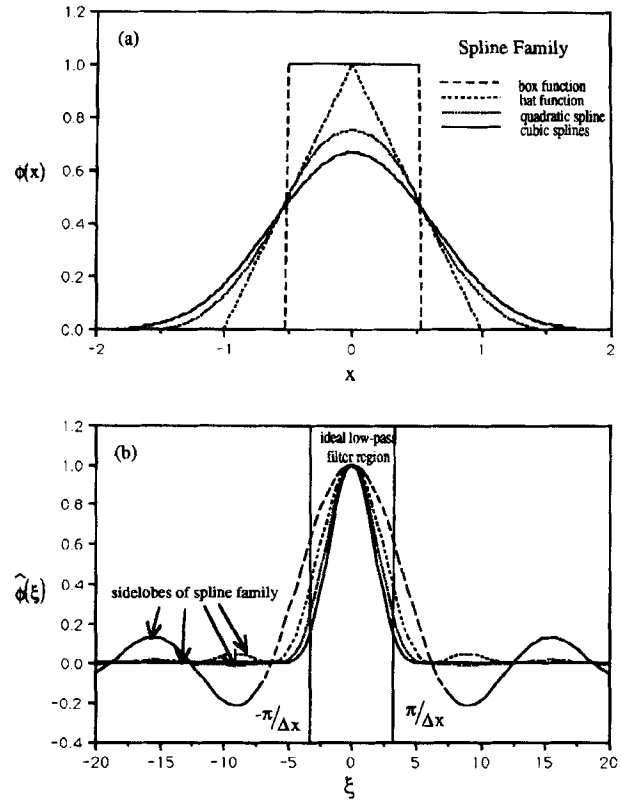

Figure 5. (a) Four spline functions (for $a_0 = 1$): box function, hat function, quadratic spline and cubic spline. (b) Their Fourier transforms

domain decrease as the order of the window function increases. This decrease in side-lobe will prevent additional high frequency aliasing from being introduced into the system response.

For a given window function (usually in terms of polynomials) *the number of nodes covered under the support can be determined with this choice of optimal dilation parameters to yield the optimal rate of convergence as well as absolute accuracy.* Another way to interpret this result is as the best match of the number of nodes with the order of the global shape function, which is related to the window function used.

Table II. Spline family

	$a_0\pi/\Delta x$			
dE/E (%)	Box	Hat	Quadratic	Cubic
0·001	63770·97	46·582800	10·458865	12·58643
0·01	6367·642	21·772318	8·422090	6·525427
0·1	637·1728	9·779085	4·160637	**3·565031**
1	64·62777	4·080620	3·358089	2·822957
10	5·331476	2·66750320	2·216856	1·829333
20	3·360553	2·102112	1·742766	1·248679

4.2. hp-like adaptivity by inserting nodes and translation and dilation of a single scaling function

It is noted that the choice of an optimal dilation parameter of a given window function is analogous to choosing the optimal order of the polynomial resulting from the multiple scale RKPM. It is shown in Reference 1 that *by changing the size of 'a', the refinement or dilation parameter of a single window function*, the rate of convergence of the L_2-norm (H_1-norm) of a smooth Laplacian solution varies from 2 to 16 (from 1 to 15) for a Gaussian window and from 2 to 5 (from 1 to 4) for a cubic spline window. This shows that the multiple scale RKPM has a *similar* feature of the adaptive p-finite element methods. However, the higher convergence rate, or equivalently the high value of p, can be achieved simply by increasing the size of the refinement parameter of a *single* window function. This avoids the awkward implementation of the traditional p-finite elements and there is no apprehension of the compatibility (or continuity) along the element boundaries of the hp-finite element mesh, since RKPM requires only a set of nodes and the global shape functions can be C^∞!

As in p-finite element methods, exponential convergence of smooth solutions can be achieved for this class of multiple scale RKPMs. However, if there is a discontinuity in the solution, e.g. a shock, the high convergence behaviour is lost. h-like adaptive reproducing kernel particle methods, comparable with the h-finite element method, can be developed by inserting nodes in the high gradient region and *at the same time narrowing the size of the window function (i.e. a smaller 'a') to pick up the fine scale structure of the response*. This zooming-in process together with the addition of nodes will result in an *hp-like adaptive refinement algorithm*.

Based on the multiple scale decomposition and the highest wavelet scale response, a convergence parameter or an error estimation indicator as defined in Section 4.3 can be employed to locate the adaptivity regions. In our numerical examples the refinement parameter is chosen to be the optimal parameter and the adaptive mesh parameter (Δx and Δy) are chosen to be proportional to the square root of the nodal area multiplied by the *initial 'mesh' size h* (initial Δx and Δy). A summary of the similarities between the hp-adaptive finite element method and the multiple scale reproducing kernel particle method is given in Table III.

It is further emphasized that the hp-finite element method requires the creation of an hp-mesh, and low and higher order element shape functions need to be fabricated so that the different order elements along element boundaries are compatible, whereas in the multiple scale reproducing kernel particle method the hp-equivalent adaptive refinement is a built-in condition. The adaptive refinement is accomplished by a *single p-order* (or C^∞) flexible space–scale window function that translates and dilates covering all the nodes, including those inserted along the sharp gradient regions, in the computational domain.

Table III. Similarities between hp-adaptive method and multiple scale RKPM

Multiple scale RKPM	hp-Finite element method	Remarks
Small dilation parameter a	Low order shape functions	Low computational cost
Large dilation parameter a	Higher order shape functions	Higher computational cost
Variable dilation parameter a	p-Finite elements	Single flexible window function versus higher order shape functions
Inserting nodes, reduce size of dilation parameter a	Lower order h-adaptive finite elements	Nodes versus h-mesh
Inserting nodes together with flexible dilation parameter a	hp-Adaptive finite elements	Nodes with flexible window versus hp-mesh

4.3. Convergence parameter

The error norms are defined as

$$(L_2 \text{ norm})^2 = \int_\Omega \left(u^{\text{exact}} - u^{\text{h}}\right)^2 \mathrm{d}x, \tag{45a}$$

$$(H_1 \text{ norm})^2 = \int_\Omega \left(u^{\text{exact}}_{,x} - u^{\text{h}}_{,x}\right)^2 \mathrm{d}x. \tag{45b}$$

A convergence parameter ε is defined by

$$\varepsilon = \int_\Omega \frac{|u_{\text{high}}|^2}{|u_{\text{total}}|^2} \mathrm{d}\Omega, \tag{45c}$$

where u_{high} is the highest band solution from the multiple scale decomposition algorithm and u_{total} is the total solution.

5. NUMERICAL EXAMPLES

Three examples are given in this section: the Helmholtz equation (band-limited) and the 1D and 2D advection–diffusion equations (non-band-limited). For the Helmholtz and 1D advection–diffusion equations the computation is accomplished by the linear FEM (regular FEM for Helmholtz equation and stabilized FEM for advection–diffusion equation), RKPM and WPM. The linear finite element solution is computed for comparison. The RKPM is evaluated at two levels: $\mathrm{d}E/E = 8\%$ and $\mathrm{d}E/E = 0{\cdot}01\%$. See Table I for the dilation parameter a. $\mathrm{d}E/E = 8\%$ is for comparison with the finite element method and $\mathrm{d}E/E = 0{\cdot}01\%$ is to show how aliasing elimination can improve the solution. The WPM computation is performed with the finest scale ($m = 0$ in normalized formulation) scaling function. In Section 5.2 the results from the RKPM are separated into four band solutions by the multiple scale decomposition and their applications are also demonstrated. The computation of the 2D advection–diffusion equation is performed by a cubic spline window. The 2D decomposition algorithm, *hp*-like adaptive refinements and results are presented in Section 5.3.

Uniform and irregular spacings are chosen in this paper as in the nine-node example shown in Figure 6. For the irregular spacing case Δx_2 is used to derive the dilation parameter a in the RKPM and $(\Delta x_1 + \Delta x_2)/2$ is used as the normalization parameter Δx in the wavelet computation.

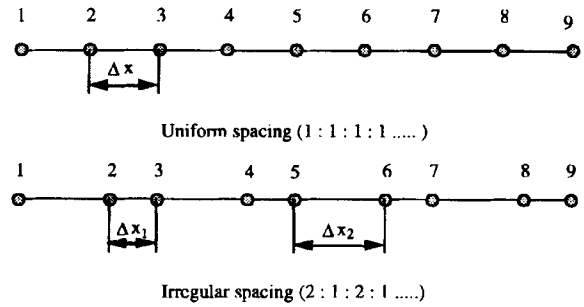

Figure 6. Different spacings used in numerical examples

5.1. Helmholtz equation

The standard 1D Helmholtz equation is given as

$$u_{,xx} + \lambda u = 0, \tag{46}$$

with boundary conditions

$$u(0) = 0, \tag{47a}$$

$$u(L) = 1. \tag{47b}$$

For $\lambda > 0$ the exact solution is given as

$$u = \frac{\sin(\sqrt{\lambda}x)}{\sin(\sqrt{\lambda}L)}. \tag{48}$$

The Fourier transform of the Helmholtz equation is a single peak, which is definitely band-limited. This single peak is located at $\sqrt{\lambda}$ in the Fourier transform domain. If the sampling rate is larger than $2\pi/\sqrt{\lambda}$, i.e. $\Delta x < 2\pi/\sqrt{\lambda}$, then this problem can be considered well-sampled.

The H_1- and L_2-norms are listed in Tables IV and V. Two interesting results can be observed.

1. Because of the side-lobe effect of the linear FEM, the Gaussian window with $dE/E = 8\%$ gives better accuracy than that of the FEM as predicted in Section 4.
2. With the same window function a smaller dE/E ratio gives better absolute accuracy, but with similar convergence rates.

5.2. 1D advection–diffusion equation

The steady state advection–diffusion problem can be stated for the one-dimensional case as

$$u_{,xx} - \alpha u_{,x} = b(x) \quad \text{in } \Omega, \tag{49}$$

with boundary conditions

$$u(x_g) = u_1 \quad \text{on } \Gamma_g, \tag{50a}$$

Table IV. (a) Error in numerical solution of Helmholtz equation ($\sqrt{\lambda} = 1{\cdot}2\pi$) in uniform spacing case

	9 nodes	17 nodes	33 nodes	65 nodes
Finite element method	0·777306	0·450348	0·178571	$5{\cdot}238338 \times 10^{-2}$
Wavelet particle method	0·77731	0·45035	0·17857	$5{\cdot}23833 \times 10^{-2}$
RKPM, $dE/E = 8\%$	0·66821	0·32202	0·10112	$2{\cdot}69610 \times 10^{-2}$
RKPM, $dE/E = 0{\cdot}01\%$	$4{\cdot}415052 \times 10^{-2}$	$1{\cdot}805416 \times 10^{-3}$	$3{\cdot}764297 \times 10^{-4}$	$7{\cdot}070435 \times 10^{-5}$

Table IV. (b) Error in first derivative of numerical solution of Helmholtz equation ($\sqrt{\lambda} = 1{\cdot}2\pi$) in uniform spacing case

	9 nodes	17 nodes	33 nodes	65 nodes
Finite element method	0·859291	0·509883	0·224066	$8{\cdot}715449 \times 10^{-2}$
Wavelet particle method	0·85929	0·50988	0·22407	$8{\cdot}71545 \times 10^{-2}$
RKPM, $dE/E = 8\%$	0·74062	0·37557	0·14177	$5{\cdot}64656 \times 10^{-2}$
RKPM, $dE/E = 0{\cdot}01\%$	$5{\cdot}798656 \times 10^{-2}$	$7{\cdot}885859 \times 10^{-3}$	$3{\cdot}215679 \times 10^{-3}$	$1{\cdot}208999 \times 10^{-3}$

Table V. (a) Error in numerical solution of Helmholtz equation ($\sqrt{\lambda} = 1{\cdot}2\pi$) in irregular spacing case

	9 nodes	17 nodes	33 nodes	65 nodes
Finite element method	2·748756	0·498553	0·218961	$6{\cdot}750198 \times 10^{-2}$
Wavelet particle method	0·803013	0·450663	0·199713	$5{\cdot}282151 \times 10^{-2}$
RKPM, $dE/E = 8\%$	1·022333	0·353102	0·136492	$6{\cdot}764163 \times 10^{-2}$
RKPM, $dE/E = 0{\cdot}01\%$	$3{\cdot}585980 \times 10^{-2}$	$5{\cdot}536716 \times 10^{-3}$	$1{\cdot}192248 \times 10^{-3}$	$3{\cdot}785657 \times 10^{-4}$

Table V. (b) Error in first derivative of numerical solution of Helmholtz equation ($\sqrt{\lambda} = 1{\cdot}2\pi$) in irregular spacing case

	9 nodes	17 nodes	33 nodes	65 nodes
Finite element method	3·042870	0·568192	0·263465	0·100213
Wavelet particle method	0·861549	0·529122	0·229015	$8{\cdot}788850 \times 10^{-2}$
RKPM, $dE/E = 8\%$	1·087927	0·406603	0·193244	$6{\cdot}764163 \times 10^{-2}$
RKPM, $dE/E = 0{\cdot}01\%$	$6{\cdot}386343 \times 10^{-2}$	$1{\cdot}877033 \times 10^{-2}$	$8{\cdot}186295 \times 10^{-3}$	$4{\cdot}760357 \times 10^{-3}$

$$u_{,x}(x_h) = u_2' \quad \text{on } \Gamma_h, \tag{50b}$$

where Ω is the domain (i.e. $0 \leqslant x \leqslant L$), Γ_g is the essential boundary condition and Γ_h is the natural boundary condition. The boundary is $\Gamma = \Gamma_g \cup \Gamma_h$ and $\Gamma_g \cap \Gamma_h = \{\varnothing\}$; $(\cdot)_{,x}$ denotes the derivative with respect to x, u is the scalar unknown, α is a given constant and $b(x)$ is a given source term. The parameter α is the advective velocity divided by the diffusion coefficient. The Peclet number is therefore

$$Pe = \frac{\alpha \Delta x}{2}. \tag{50c}$$

The source term $b(x)$ can be caused by a chemical reaction. Following Hughes *et al.*,[8] the weak form of equation (49) with the least square term can be written as

$$\int_\Omega w(u_{,xx} - \alpha u_{,x} - b)\, d\Omega + \int_\Omega (w_{,xx} - \alpha w_{,x})\tau(u_{,xx} - \alpha u_{,x} - b)\, d\Omega = 0, \tag{51}$$

where w is an arbitrary test function and τ is a parameter. Using the approximation u^h and w^h for the functions u and w, we obtain the usual matrix equation. The choice of τ depends on the parameter α and the nodal distance $\Delta x_k = x_{k+1} - x_k$. For the advection–dominated case an estimation of τ is given by[8]

$$\tau = \frac{\Delta x}{2\alpha} \tag{52a}$$

or[9]

$$\tau = \left[\left(\frac{2\alpha}{\Delta x} \right)^2 + 9 \left(\frac{4\kappa}{\Delta x^2} \right)^2 \right]^{1/2}, \tag{52b}$$

where α is the advection coefficient introduced earlier, κ. is the diffusion coefficient and Δx is the nodal distance. We are currently investigating a sharper estimation of τ for the RKPM.

The following numerical examples use a highly irregular source term to produce a non-linear solution with two peaks. The source term consists of two terms that are very similar and summed together. Each part is

$$b_i(x) = \frac{2c_{1i}c_{2i}e^{c_{2i}(x-x_{0i})}(e^{2c_{2i}(x-x_{0i})}-1)\operatorname{sech}^2[c_{1i}(x-x_{0i})]}{(e^{2c_{2i}(x-x_{0i})}+1)^2}$$

$$+\frac{2c_{1i}^2\operatorname{sech}[c_{1i}(x-x_{0i})]^2\tanh[c_{1i}(x-x_{0i})]}{e^{c_{2i}(x-x_{0i})}+e^{-c_{2i}(x-x_{0i})}}-\frac{c_{2i}^2(e^{c_{2i}(x-x_{0i})}+e^{-c_{2i}(x-x_{0i})})\{1-\tanh[c_{1i}(x-x_{0i})]\}}{(e^{c_{2i}(x-x_{0i})}+e^{-c_{2i}(x-x_{0i})})^2}$$

$$+\frac{2c_{2i}^2(e^{c_{2i}(x-x_{0i})}-e^{-c_{2i}(x-x_{0i})})^2\{1-\tanh[c_{1i}(x-x_{0i})]\}}{(e^{c_{2i}(x-x_{0i})}+e^{-c_{2i}(x-x_{0i})})^3}$$

$$+\alpha\frac{c_{2i}(e^{c_{2i}(x-x_{0i})}-e^{-c_{2i}(x-x_{0i})})\{1-\tanh[c_{1i}(x-x_{0i})]\}}{(e^{c_{2i}(x-x_{0i})}+e^{-c_{2i}(x-x_{0i})})^2}$$

$$+\alpha\frac{c_{1i}\operatorname{sech}[c_{1i}(x-x_{0i})]^2}{e^{c_{2i}(x-x_{0i})}+e^{-c_{2i}(x-x_{0i})}}, \tag{53}$$

where x_{0i} governs the position of the peak, c_{1i} controls the sharpness on the right side of the peak and c_{2i} controls the decay on the left side. The resulting source term is

$$b(x) = k_1 b_1(x) + k_2 b_2(x), \tag{54}$$

with the parameters

	$i=1$	$i=2$
x_{0i}	1·7	3·2
c_{1i}	50	50
c_{2i}	4·0	5·0
k_i	0·5	1·0

where the parameter k determines the size of the peak. The source term using these coefficients is shown in Figure 7.

The homogeneous solution of the advection–diffusion equation in the domain $0 \leqslant x \leqslant 4$ with boundary conditions $u(0) = 0$ and $u(4) = 1$ becomes

$$u^{\mathrm{H}}(x) = \frac{e^{\alpha x}-1}{e^{4\alpha}-1}. \tag{55}$$

The particular solution produced by $b(x)$ is given by

$$u^{\mathrm{P}}(x) = k_1 u_1^{\mathrm{P}}(x) + k_2 u_2^{\mathrm{P}}(x), \tag{56}$$

where

$$u_i^{\mathrm{P}}(x) = \frac{1-\tanh[c_{1i}(x-x_{0i})]}{e^{c_{2i}(x-x_{0i})}+e^{-c_{2i}(x-x_{0i})}}, \quad i=1,2, \tag{57}$$

with the appropriate constants from the table above. The parameter α is set to 50.

The computed solutions of the advection–diffusion equation using several different methods are shown in Figures 8–10 (uniform spacing). For this non-band-limited problem the RKPM with the

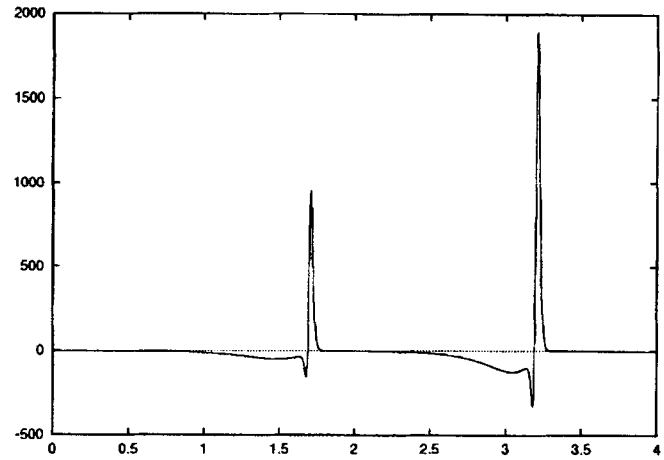

Figure 7. Source term used in 1D advection–diffusion equation

smaller dE/E ratio shows very high absolute accuracy and a superior convergence rate. From Figure 8, oscillations occur in the small dE/E ratio case when the mesh is coarse. After adding high frequency wavelet bands, these oscillations are eliminated. For uniform nodal spacing the WPM shows a convergence rate and absolute accuracy identical with those of the stabilized FEM, but in the irregular spacing case the WPM has better performance than that of the stabilized FEM. The fast Fourier transform (FFT) of the system response is depicted in Figure 9 along with the applied window used in this decomposition. Figure 10 shows that the contribution of the highest band solution becomes less significant as the spacing becomes finer and finer. Both Figures 9 and 10 show that this highest band solution can be a good indicator for local mesh refinement. Tables VI and VII display the superior convergence of the RKPM. Figure 11 and Table VIII show that the error indicator parameter ε is indeed a good index to examine the convergence of the solution.

Table VI. (a) Error in numerical solution of 1D advection–diffusion equation in uniform spacing case

	33 nodes	65 nodes	129 nodes	257 nodes
Finite element method	0·334955	0·214855	0·106109	$5{\cdot}925850 \times 10^{-2}$
Wavelet particle method	0·336132	0·214906	0·106589	$5{\cdot}933086 \times 10^{-2}$
RKPM, $dE/E = 8\%$	0·322079	0·207193	0·104550	$6{\cdot}431538 \times 10^{-2}$
RKPM, $dE/E = 0{\cdot}01\%$	0·267828	0·118584	$3{\cdot}107031 \times 10^{-2}$	$8{\cdot}088636 \times 10^{-3}$

Table VI. (b) Error in first derivative of numerical solution of 1D advection–diffusion equation in uniform spacing case

	33 nodes	65 nodes	129 nodes	257 nodes
Finite element method	0·785792	0·645285	0·407359	0·271882
Wavelet particle method	0·785879	0·645292	0·407700	0·272002
RKPM, $dE/E = 8\%$	0·765642	0·639221	0·409797	0·308105
RKPM, $dE/E = 0{\cdot}01\%$	0·695062	0·464779	0·161893	$4{\cdot}722526 \times 10^{-2}$

Table VII. (a) Error in numerical solution of 1D advection–diffusion equation in irregular spacing case

	33 nodes	65 nodes	129 nodes	257 nodes
Finite element method	0·296929	0·1880530	$8{\cdot}329611 \times 10^{-2}$	$4{\cdot}000011 \times 10^{-2}$
Wavelet particle method	0·313160	0·168621	$5{\cdot}743446 \times 10^{-2}$	$2{\cdot}469355 \times 10^{-2}$
RKPM, $dE/E = 0{\cdot}01\%$	0·238021	$8{\cdot}280159 \times 10^{-2}$	$1{\cdot}501983 \times 10^{-2}$	$4{\cdot}403418 \times 10^{-3}$

Table VII. (b) Error in first derivative of numerical solution of 1D advection–diffusion equation in irregular spacing case

	33 nodes	65 nodes	129 nodes	257 nodes
Finite element method	0·671608	0·617237	0·375262	0·224363
Wavelet particle method	0·744976	0·611346	0·361955	0·216244
RKPM, $dE/E = 0{\cdot}01\%$	0·584714	0·337591	0·111176	$1{\cdot}173159 \times 10^{-2}$

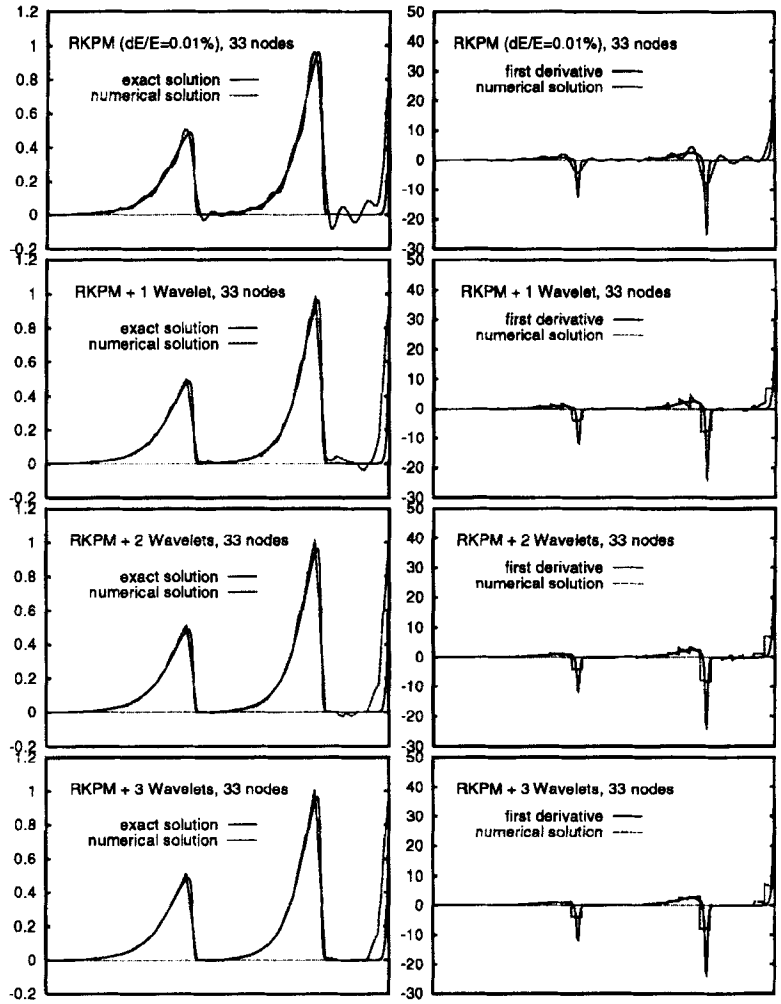

Figure 8. Solution of advection–diffusion equation by RKPM ($dE/E = 0{\cdot}01\%$) with wavelets

Table VIII. Error estimation parameter using multiple scale RKPM

	33 nodes	65 nodes	129 nodes	257 nodes
ε (multiple scale RKPM)	0·217100	$8{\cdot}9765 \times 10^{-2}$	$3{\cdot}1887 \times 10^{-2}$	$9{\cdot}6386 \times 10^{-3}$

5.3. *2D advection–diffusion equation*

The steady state 2D advection–diffusion equation is given as

$$v\nabla^2\phi - \mathbf{u}\cdot\nabla\phi = 0. \tag{58}$$

The problem statement is depicted in Figure 12. The flow is unidirectional, constant ($\| \mathbf{u} \| = 1$) and skew to the mesh. The diffusivity coefficient v is taken to be 10^{-6}. The inflow boundary condition is discontinuous, as shown, and a natural boundary condition is applied to the outflow boundary. The

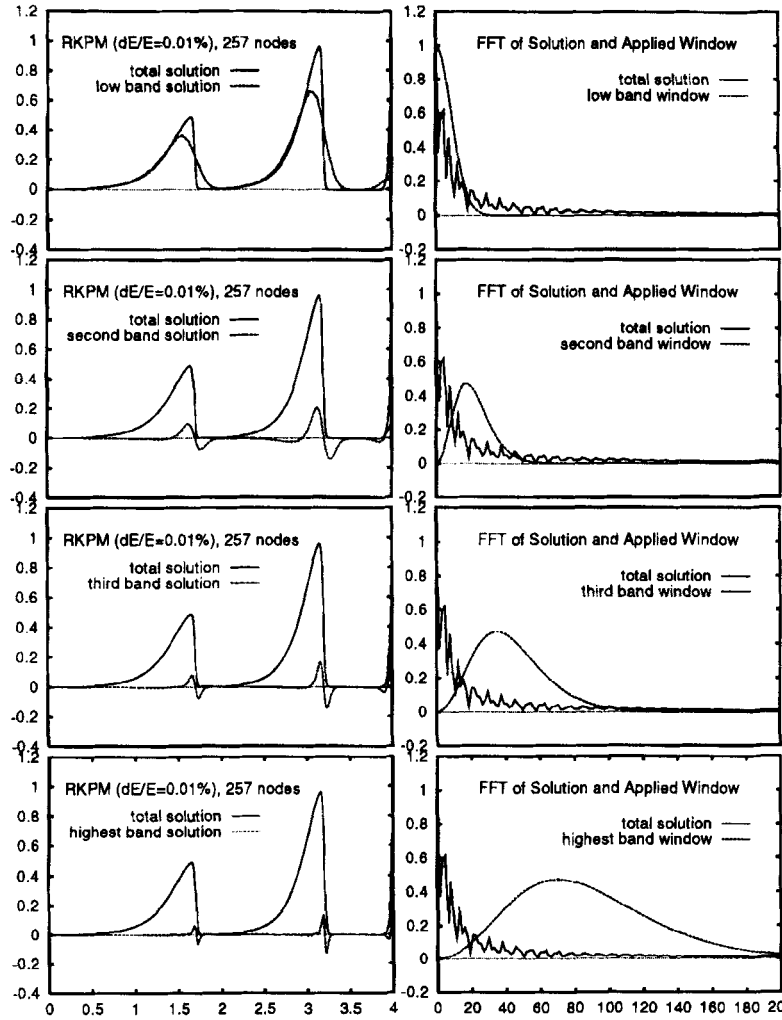

Figure 9. Four-band decomposition of total solution by multiscale RKPM decomposition algorithm

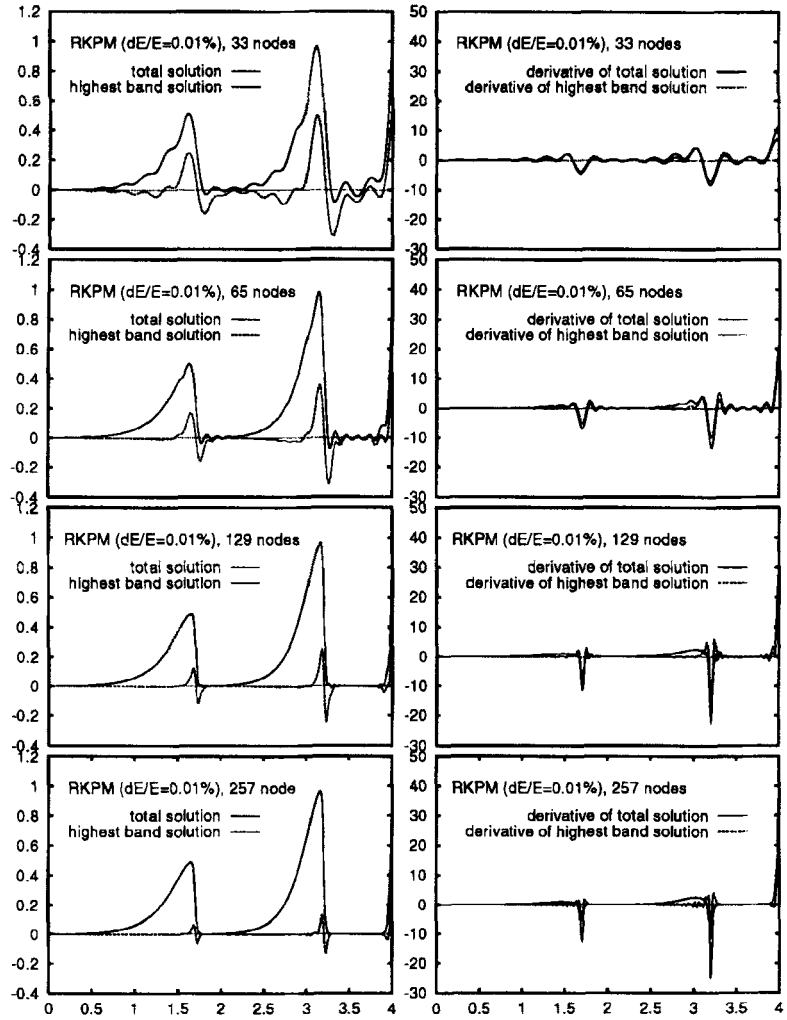

Figure 10. Highest band solution from multiscale RKPM can be used as reference for local mesh refinement

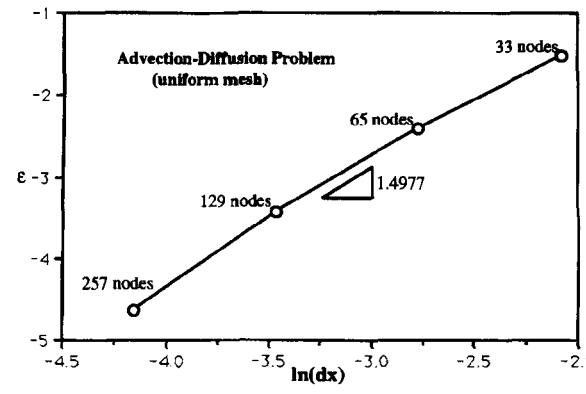

Figure 11. Convergence plot of error estimation parameter ε using multiscale RKPM

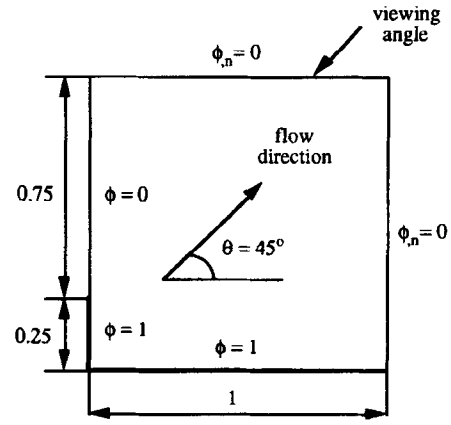

Figure 12. Advection skew to mesh: problem statement

cubic spline is the kernel function and its energy error ratio dE/E is chosen as 0·1% for all cases. See Table II for the dilation parameter a. Four uniform refinements, 11 × 11, 21 × 21, 41 × 41 and 61 × 61 nodes, are used to compute the results. In addition, two adaptive refinements based on a 3 × 3 multiple scale decomposition of the 21 × 21 grid are performed.

The 2D RKPM is given as

$$u(x,y)=\int_{\nu} C(x,y,\bar{x},\bar{y},a_{x0},a_{y0})\phi\left(\frac{x-\bar{x}}{a_{x0}},\frac{y-\bar{y}}{a_{y0}}\right)u(\bar{x},\bar{y})\,d\bar{x}\,d\bar{y}, \tag{59}$$

where $C(x,y,\bar{x},\bar{y},a_{x0},a_{y0})$ is the boundary correction for the finite domain and

$$\phi\left(\frac{x-\bar{x}}{a_{x0}},\frac{y-\bar{y}}{a_{y0}}\right)=\phi\left(\frac{x-\bar{x}}{a_{x0}}\right)\phi\left(\frac{y-\bar{y}}{a_{y0}}\right)$$

is the cross-product of two 1D window functions. The n-level decomposition specified by the window functions is given as

$$\phi_0(x,y)=\psi_1(x)\psi_1(y)+\cdots+\psi_2(x)\psi_2(y)+\cdots+\phi_n(x)\phi_n(y). \tag{60}$$

In the Fourier transform domain an example of three-level decomposition is given as

$$\begin{aligned}\hat{\phi}_0(\xi,\eta)&=\hat{\phi}_0(\xi)\hat{\phi}_0(\eta)\\&=[\hat{\phi}_2(\xi)+\hat{\psi}_2(\xi)+\hat{\psi}_1(\xi)][\hat{\phi}_2(\eta)+\hat{\psi}_2(\eta)+\hat{\psi}_1(\eta)]\\&=\hat{\phi}_2(\xi)\hat{\phi}_2(\eta)+\hat{\phi}_2(\xi)\hat{\psi}_2(\eta)+\hat{\phi}_2(\xi)\hat{\psi}_1(\eta)\\&\quad+\hat{\psi}_2(\xi)\hat{\phi}_2(\eta)+\hat{\psi}_2(\xi)\hat{\psi}_2(\eta)+\hat{\psi}_2(\xi)\hat{\psi}_1(\eta)\\&\quad+\hat{\psi}_1(\xi)\hat{\phi}_2(\eta)+\hat{\psi}_1(\xi)\hat{\psi}_2(\eta)+\hat{\psi}_1(\xi)\hat{\psi}_1(\eta).\end{aligned} \tag{61}$$

The numerical results of the four uniform spacing grids (121, 441, 1681 and 3721 nodes) and the successive adaptive refinements based on the 21 × 21 grid points (472 and 514 nodes) are depicted in Figure 13. As can be seen in the figure, the results of the adaptive refinements, in which only nodes are added to the high gradient region, compare favourably with that of the 3721 nodes (61 × 61 uniform grid). The 3 × 3 decomposition plots of the 441 nodes (21 × 21 uniform grid) based on (61) and the second adaptive refinement (514 nodes) are depicted in Figure 14. The low scale (scaling function)

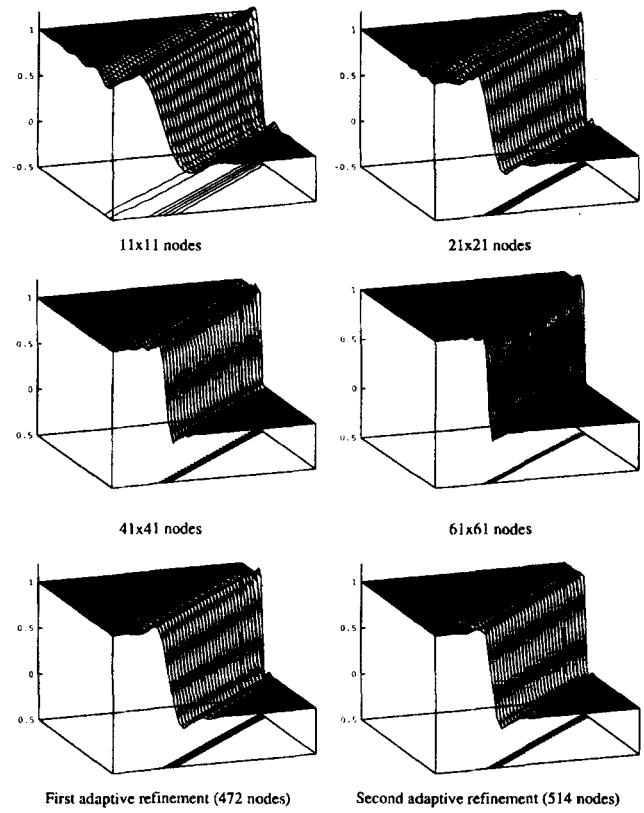

Figure 13. Numerical solutions for different refinements

component $\phi_2(x)*\phi_2(y)$ filters out the oscillation; therefore it gives a very smooth solution around the shock front. The medium and high scale (wavelets) components $\psi_2(x) * \psi_2(y)$ and $\psi_1(x) * \psi_1(y)$ show a mixture of high wave number response and aliasing. However, the medium scale displays mostly the high wave number approximation of the shock front whereas the high scale displays mostly the aliasing wave number that cannot be resolved with a 514-node resolution. This is a typical example of the Gibbs phenomenon. Nevertheless, the high wavelet component $\psi_1(x) * \psi_1(y)$ picks up the location of the high gradient region. We are currently investigating the optimal level of multiple scale decomposition in defining adaptivity.

Comparing the two sets of multiple scale decomposition depicted in Figure 14, the adaptive refinement locates the shock front more precisely than that of 21×21 nodes. This is clearly illustrated in the $\psi_1(x) * \psi_1(y)$ wavelet components, in which the magnitude of the aliasing solution and the width of the shock are much smaller. In the same figure the adaptive low scale (scaling function) component $\phi_2(x) * \phi_2(y)$ gives a better approximation of the discontinuous solution than that of the uniform mesh. Figure 15 shows the location of the adaptive refinements. The 50 highest nodal values (about 10% of the total number of nodes) of the $\psi_1(x) * \psi_1(y)$ wavelet (high wave number) components are chosen to locate the high gradient region. Thirty-one nodes are added in this region in the first adaptive refinement. A similar 3×3 decomposition is also applied to the total solution of the first adaptive refinement. Based on this new high gradient region, an additional 42 nodes are added to achieve the second adaptive refinement. One should note that in Figure 15 not only does the width of the high gradient region become narrower, but also its maximum value decreases from 0·907 to 0·657 when the

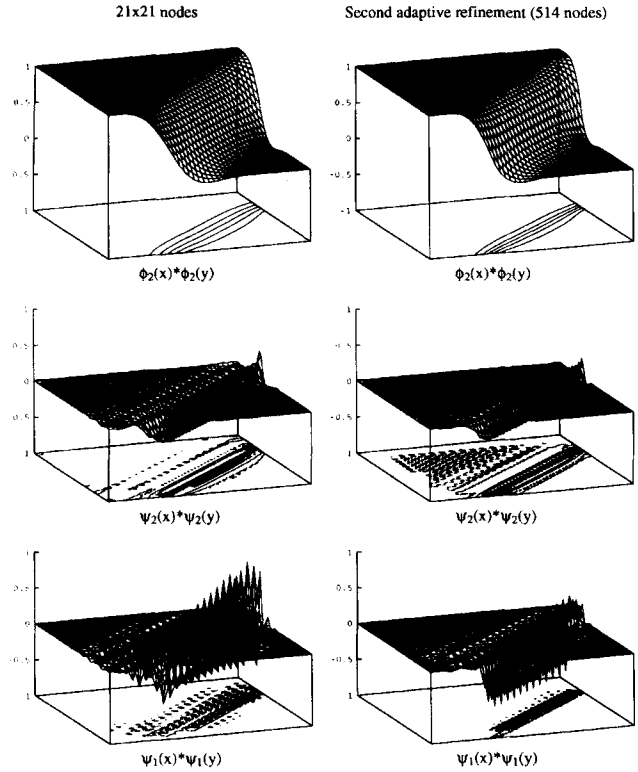

Figure 14. Plots of 3 × 3 decomposition of total solution

adaptive refinements are applied. This example shows that the integral window transform process can zoom in to pick up the high gradient of the response and zoom out if no magnification of the response is necessary. The zoom-in and zoom-out capability of the multiple scale reproducing kernel method shows great promise for meshless unstructured multigrid or *hp*-like adaptivity. Moreover, the physical interpretation of the computed results can be further synthesized.

6. CONCLUSIONS

Reproducing kernel and wavelet particle methods, as shown in the numerical examples, provide accurate mesh-free interpolation functions that possess superior convergence rate. The wavelet particle method, which combines wavelet analysis and particle methods, allows us to separate the response into multiple frequency/wave number bands via a multiresolution analysis. Through the integral window transform and the dilation and translation of the scaling function, the window function can magnify, examine and record the image of the various scales (frequencies and wave numbers) of the response locally within the support of the window function. Hence the multiple scale RKPM can provide a good physical interpretation of the computed response. Also, the concept of multiresolution, which is a built-in property of the multiple scale RKPM, provides a firm foundation in the construction of algorithms for unstructured *hp*-like adaptive refinements without a mesh.

Aliasing control is shown to be very important in improving the accuracy and convergence rate of the discretized solution. Without the exact solution for a given system we are able to set up criteria for the convergence of the computed solution. Moreover, adaptive refinement criteria have been developed with the help of these multiple scale methods. In this adaptive refinement procedure, nodes are simply

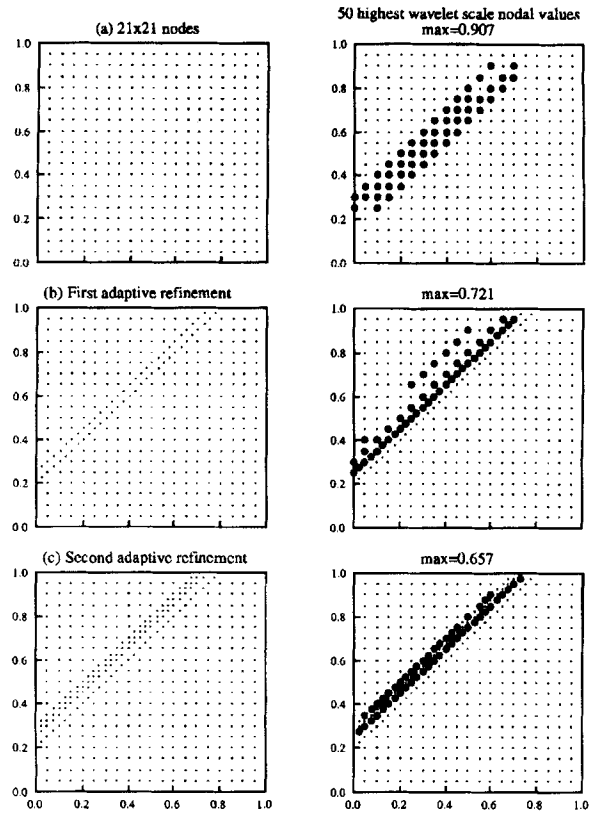

Figure 15. Adaptive refinement by 3 × 3 multiple scale decomposition: (a) 441 nodes; (b) 472 nodes; (c) 514 nodes

inserted to selected wavelet regions of high gradients, but without a mesh or a grid. In addition, the size of the window function is narrowed to examine the finer scales of the response.

An energy error ratio criterion is also developed via Fourier analysis of the kernel window function of the RKPM. Optimal dilation parameters have been established for a class of window functions that give high convergence rates as well as optimal aliasing control of unwanted numerical frequencies/ wave numbers. This optimal aliasing control dilation parameter will dictate the best match between the number of nodes used for this scaling function, i.e. the optimal number of nodes covered within the support of the window function.

One of the key successes of this class of particle methods is the formulation of the boundary correction function to scaling functions and wavelets. Hence, unlike the usual wavelet analysis, no

Table IX. Linear scaling function coefficients

n	a_n	b_n	x
1	0·745749187	−0·84659105	$0 \leqslant x \leqslant 1$
2	−0·10084186	0·12117043	$1 \leqslant x \leqslant 2$
3	0·020328568	−0·024874868	$2 \leqslant x \leqslant 3$
4	−0·0045463	0·0045463	$3 \leqslant x \leqslant 4$

artificial boundaries are needed in the RKPM. The role of the correction function in smooth particle hydrodynamic (SPH) methods and wavelet analysis will be discussed in a separate paper.

ACKNOWLEDGEMENT

This research is supported by ONR Grant N00014-94-1-0549.

APPENDIX I: LINEAR ORTHOGONAL WAVELETS[6,10]

The orthogonal linear wavelet derived from the orthogonal scaling function $\phi(x)$ is given in this appendix. This orthogonal scaling function is written in piecewise linear form as

$$\phi(x) = a_n + b_n(x - n + 1), \tag{62}$$

where a_n and b_n are as given in Table IX. The scaling function $\phi(x)$ is symmetric with respect to $x = 0$ and the coefficients are truncated beyond ± 4.

The corresponding linear mother wavelet is defined as

$$\psi(x) = c_n + d_n\left(x_n - \frac{n-1}{2}\right), \tag{63}$$

where c_n and d_n are as given in Table X and $x_n = x - 0{\cdot}5$. The linear mother wavelet is symmetric with respect to $x = 0{\cdot}5$ and the coefficients are truncated beyond $\pm 6{\cdot}5$.

The orthogonal linear scaling and wavelet functions are depicted in Figure 16.

APPENDIX II: MIRROR-IMAGE BOUNDARY CORRECTION METHOD

For a finite domain with boundary limit $[c_1, c_2]$ the mirror-image response outside the domain is assumed as (see Figure 17)

$$u(2c_1 - x) = u(x), \quad x \in [c_1, c_2], \quad \text{outside the left boundary,} \tag{64a}$$

$$u(2c_2 - x) = u(x), \quad x \in [c_1, c_2], \quad \text{outside the right boundary.} \tag{64b}$$

Table X. Linear mother wavelet coefficients

n	c_n	d_n	x_n
1	−1·681933641037244	5·21818612459	$0{\cdot}0 \leqslant x_n \leqslant 0{\cdot}5$
2	0·927159421260589	−1·864222673100998	$0{\cdot}5 \leqslant x_n \leqslant 1{\cdot}0$
3	−0·004951915289909663	−0·1449767598344972	$1{\cdot}0 \leqslant x_n \leqslant 1{\cdot}5$
4	−0·07744029520715825	0·1073186691880838	$1{\cdot}5 \leqslant x_n \leqslant 2{\cdot}0$
5	−0·02378096061311632	0·0868434903891853	$2{\cdot}0 \leqslant x_n \leqslant 2{\cdot}5$
6	0·01964078458147631	−0·02999996523471812	$2{\cdot}5 \leqslant x_n \leqslant 3{\cdot}0$
7	0·00464080196411725	−0·01753474565417041	$3{\cdot}0 \leqslant x_n \leqslant 3{\cdot}5$
8	−0·004126570862967956	0·005851168536231734	$3{\cdot}5 \leqslant x_n \leqslant 4{\cdot}0$
9	−0·00120098659485209	0·004375170028290078	$4{\cdot}0 \leqslant x_n \leqslant 4{\cdot}5$
10	0·000986598419292949	−0·001444613137703367	$4{\cdot}5 \leqslant x_n \leqslant 5{\cdot}0$
11	0·000262429185044126 57	−0·000580723064841730 2	$5{\cdot}0 \leqslant x_n \leqslant 5{\cdot}5$
12	−0·000026069681979599 4	0·000061477633891292 45	$5{\cdot}5 \leqslant x_n \leqslant 6{\cdot}0$
13	$4{\cdot}669134966046848 \times 10^{-6}$	$-9{\cdot}338268 \times 10^{-6}$	$6{\cdot}0 \leqslant x_n \leqslant 6{\cdot}5$

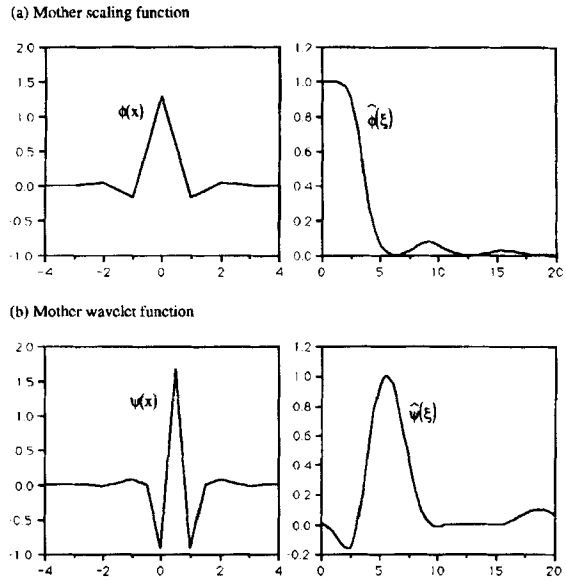

Figure 16. Orthogonal scaling and wavelet functions and their Fourier transforms

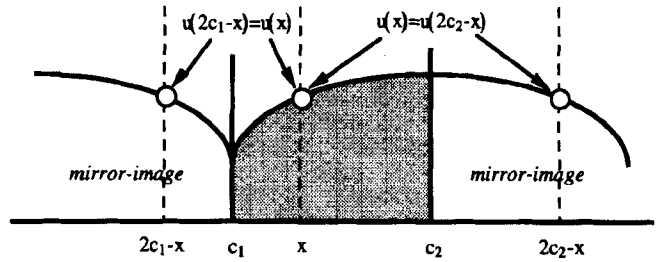

Figure 17. Application of mirror-image outside domain of response

The reproducing kernel integral can be shown to be

$$\int_{-\infty}^{\infty} u(y)\phi(x-y)\,dy = \int_{-\infty}^{c_1} u(y)\phi(x-y)\,dy + \int_{c_1}^{c_2} u(y)\phi(x-y)\,dy + \int_{c_2}^{\infty} u(y)\phi(x-y)\,dy. \tag{65}$$

Using equations (64), the first and third terms of (65) are shown to be

$$\int_{-\infty}^{c_1} u(y)\phi(x-y)\,dy = \int_{c_1}^{c_2} u(y)\phi(x-2c_1+y)\,dy + \int_{c_2}^{\infty} u(y)\phi(x-2c_1+y)\,dy, \tag{66a}$$

$$\int_{c_2}^{\infty} u(y)\phi(x-y)\,dy = \int_{c_1}^{c_2} u(y)\phi(x-2c_2+y)\,dy + \int_{-\infty}^{c_1} u(y)\phi(x-2c_2+y)\,dy. \tag{66b}$$

Examining the second term on the RHS of (66a), if the support of $\phi(x-2c_1+y)$ is small, this term becomes an empty set in the interval $[c_1, \infty)$ and hence it is zero. A similar argument can be applied to

the second term on the RHS of (66b). Therefore these two terms can be dropped. Substituting equations (66) into (65), the kernel function becomes

$$u^{\mathrm{h}}(x) = \int_{c_1}^{c_2} u(y)\tilde{\phi}(x-y)\,\mathrm{d}y, \tag{67}$$

where

$$\tilde{\phi}(x-y) = \phi(x-y) + \phi(x-2c_1+y) + \phi(x-2c_2+y). \tag{68}$$

The new shape function is

$$N_i(x) = [\phi(x-2c_1+x_i) + \phi(x-x_i) + \phi(x-2c_2+x_i)]\Delta x_i. \tag{69}$$

The boundary correction terms for the WPM can be derived in a similar manner to those of RKPM.

APPENDIX III: SPLINE FAMILY

Define the convolution of two functions as

$$(f * g)(x) = \int f(y)g(x-y)\,\mathrm{d}y, \tag{70}$$

where $*$ denotes the convolution of two functions.

The convolution of any two members from the spline family will produce a higher order spline function of the same spline family. Starting from a simple box function, the whole spline family can be constructed through a recursive convolution algorithm. From the convolution theorem

$$F(f * g) = F(f)F(g), \tag{71}$$

where $F(.)$ is the Fourier transform operator, the Fourier transforms of the spline family can be derived automatically.

Box function

$$\phi\left(\frac{x}{a}\right) = \begin{cases} 1/a, & -\frac{1}{2} \leqslant x/a \leqslant \frac{1}{2}, \\ 0, & \text{otherwise}, \end{cases} \tag{72a}$$

$$\hat{\phi}(a\xi) = \frac{\sin(a\xi/2)}{a\xi/2}, \tag{72b}$$

$$\frac{\mathrm{d}E}{E} = 1 - \frac{1}{\pi} f\left(\frac{a\pi}{\Delta x}\right), \tag{72c}$$

where

$$f(\xi) = -\frac{2}{\xi} + \frac{2}{\xi}\cos(\xi) + 2\mathrm{Si}(\xi), \tag{72d}$$

with

$$\mathrm{Si}(\xi) = \int_0^{\xi} \frac{\sin(\eta)}{\eta}\,\mathrm{d}\eta. \tag{72e}$$

*Hat function = box * box*

$$\phi\left(\frac{x}{a}\right) = \begin{cases} x/a + 1, & -1 \leqslant x/a \leqslant 0, \\ -x/a + 1, & 0 \leqslant x/a \leqslant 1, \\ 0, & \text{otherwise}, \end{cases} \tag{73a}$$

$$\hat{\phi}(a\xi) = \left(\frac{\sin(a\xi/2)}{a\xi/2}\right)^2, \tag{73b}$$

$$\frac{dE}{E} = 1 - \frac{3}{2\pi} f\left(\frac{a\pi}{\Delta x}\right), \tag{73c}$$

where

$$\begin{aligned} f(\xi) = &-\frac{4}{3}\frac{1}{\xi^3} - \frac{4}{3}\frac{1}{\xi^3}\cos^2(\xi) + \frac{8}{3}\frac{1}{\xi^3}\cos(\xi) + \frac{4}{3}\frac{1}{\xi^2}\sin(\xi)\cos(\xi) \\ &-\frac{4}{3}\frac{1}{\xi^2}\sin(\xi) - \frac{4}{3}\,\mathrm{Si}(\xi) + \frac{8}{3}\frac{1}{\xi}\cos^2(\xi) - \frac{4}{3}\frac{1}{\xi} - \frac{4}{3}\frac{1}{\xi}\cos(\xi) + \frac{8}{3}\,\mathrm{Si}(2\xi). \end{aligned} \tag{73d}$$

*Quadratic spline = box * hat*

$$\phi\left(\frac{x}{a}\right) = \begin{cases} \dfrac{1}{8a}\left[2\left(\dfrac{x}{a}\right) + 3\right]^2, & -\dfrac{3}{2} \leqslant \dfrac{x}{a} \leqslant -\dfrac{1}{2}, \\ \dfrac{1}{a}\left[-\left(\dfrac{x}{a}\right)^2 + \dfrac{3}{4}\right], & -\dfrac{1}{2} \leqslant \dfrac{x}{a} \leqslant \dfrac{1}{2}, \\ \dfrac{1}{8a}\left[2\left(\dfrac{x}{a}\right) - 3\right]^2, & \dfrac{1}{2} \leqslant \dfrac{x}{a} \leqslant \dfrac{3}{2}, \\ 0, & \text{otherwise}, \end{cases} \tag{74a}$$

$$\hat{\phi}(a\xi) = \left(\frac{\sin(a\xi/2)}{a\xi/2}\right)^3, \tag{74b}$$

$$\frac{dE}{E} = 1 - \frac{20}{11\pi} f\left(\frac{a\pi}{\Delta x}\right), \tag{74c}$$

where

$$\begin{aligned} f(\xi) = &-\frac{1}{5}\frac{1}{\xi^2}\sin(\xi) + \frac{24}{5}\frac{1}{\xi^5}\cos(\xi) - \frac{8}{5}\frac{1}{\xi^5} + \frac{9}{5}\frac{1}{\xi^2}\sin(\xi)\cos^2(\xi) \\ &-\frac{6}{5}\frac{1}{\xi^4}\sin(\xi)\cos^2(\xi) + \frac{12}{5}\frac{1}{\xi^4}\sin(\xi)\cos(\xi) - \frac{8}{5}\frac{1}{\xi^2}\sin(\xi)\cos(\xi) - \frac{16}{5}\frac{1}{\xi}\cos^2(\xi) \\ &+\frac{8}{5}\frac{1}{\xi} - \frac{4}{5}\frac{1}{\xi^3} - \frac{6}{5}\frac{1}{\xi^3}\cos^3(\xi) + \frac{8}{5}\frac{1}{\xi^3}\cos^2(\xi) - \frac{24}{5}\frac{1}{\xi^5}\cos^2(\xi) \\ &+\frac{8}{5}\frac{1}{\xi^5}\cos^3(\xi) + \frac{81}{20}\,\mathrm{Si}(3\xi) + \frac{1}{4}\,\mathrm{Si}(\xi) + \frac{27}{5}\cos^3(\xi) - \frac{16}{5}\,\mathrm{Si}(2\xi) \\ &-\frac{6}{5}\frac{1}{\xi^4}\sin(\xi) + \frac{2}{5}\frac{1}{\xi^3}\cos(\xi) - \frac{19}{5}\cos(\xi). \end{aligned} \tag{74d}$$

*Cubic = hat * hat = box * quadratic*

$$\phi\left(\frac{x}{a}\right)=\begin{cases}\dfrac{1}{6a}\left[\left(\dfrac{x}{a}\right)+2\right]^3, & -2\leqslant\dfrac{x}{a}\leqslant-1,\\[2ex] \dfrac{1}{a}\left[\dfrac{2}{3}-\left(\dfrac{x}{a}\right)^2\left(1+\dfrac{x}{2a}\right)\right], & -1\leqslant\dfrac{x}{a}\leqslant 0,\\[2ex] \dfrac{1}{a}\left[\dfrac{2}{3}-\left(\dfrac{x}{a}\right)^2\left(1-\dfrac{x}{2a}\right)\right], & 0\leqslant\dfrac{x}{a}\leqslant 1,\\[2ex] -\dfrac{1}{6a}\left[\left(\dfrac{x}{a}\right)-2\right]^3 & 1\leqslant\dfrac{x}{a}\leqslant 2,\\[2ex] 0, & \text{otherwise,}\end{cases}\tag{75a}$$

$$\hat{\phi}(a\xi)=\left(\frac{\sin(a\xi/2)}{a\xi/2}\right)^4,\tag{75b}$$

$$\frac{dE}{E}=1-\frac{315}{151\pi}f\left(\frac{a\pi}{\Delta x}\right),\tag{75c}$$

where

$$\begin{aligned}f(\xi)=&-\frac{32}{21}\frac{1}{\xi^6}\sin(\xi)-\frac{96}{7}\frac{1}{\xi^7}\cos^2(\xi)-\frac{16}{7}\frac{1}{\xi^7}\cos^4(\xi)-\frac{32}{35}\frac{1}{\xi^2}\sin(\xi)\cos(\xi)\\&-\frac{16}{35}\frac{1}{\xi^4}\sin(\xi)\cos(\xi)+\frac{72}{35}\frac{1}{\xi^4}\sin(\xi)\cos^2(\xi)-\frac{108}{35}\frac{1}{\xi^2}\sin(\xi)\cos^2(\xi)\\&-\frac{512}{315}\cos^4(\xi)+\frac{436}{63}\frac{1}{\xi}\cos(\xi)-\frac{472}{315}\frac{1}{\xi^3}\cos(\xi)-\frac{8}{21}\frac{1}{\xi^4}\cos^3(\xi)\\&-\frac{324}{35}\frac{1}{\xi}\cos^3(\xi)-\frac{96}{35}\frac{1}{\xi^5}\cos^3(\xi)+\frac{32}{35}\frac{1}{\xi^5}\cos^2(\xi)+\frac{32}{35}\frac{1}{\xi^3}\cos^2(\xi)\\&+\frac{72}{35}\frac{1}{\xi^3}\cos^3(\xi)-\frac{1216}{105}\frac{1}{\xi}\cos^2(\xi)+\frac{32}{21}\frac{1}{\xi^5}\cos(\xi)+\frac{236}{315}\frac{1}{\xi^2}\sin(\xi)\\&-\frac{32}{35}\frac{1}{\xi^5}+\frac{2048}{315}\operatorname{Si}(4\xi)+\frac{32}{21}\frac{1}{\xi^6}\sin(\xi)\cos^3(\xi)+\frac{32}{7}\frac{1}{\xi^6}\sin(\xi)\cos(\xi)\\&+\frac{4096}{315}\frac{1}{\xi}\cos^4(\xi)-\frac{128}{105}\frac{1}{\xi^4}\sin(\xi)\cos^3(\xi)-\frac{1}{45}\operatorname{Si}(\xi)+\frac{1024}{315}\frac{1}{\xi^2}\sin(\xi)\cos^3(\xi)\\&-\frac{32}{7}\frac{1}{\xi^6}\sin(\xi)\cos^2(\xi)+\frac{16}{105}\frac{1}{\xi^3}+\frac{32}{35}\frac{1}{\xi}+\frac{64}{45}\operatorname{Si}(2\xi)+\frac{64}{7}\frac{1}{\xi^7}\cos(\xi)\\&-\frac{16}{7}\frac{1}{\xi^7}-\frac{243}{35}\operatorname{Si}(3\xi)+\frac{64}{7}\frac{1}{\xi^7}\cos^3(\xi)+\frac{128}{105}\frac{1}{\xi^5}\cos^4(\xi).\end{aligned}\tag{75d}$$

REFERENCES

1. W. K. Liu, S. Jun and Y. F. Zhang, 'Reproducing kernel particle methods'. *Int. j. numer. methods fluids*, **20**, 1081–1106 (1995).
2. W. K. Liu, J. Adee and S. Jun, 'Reproducing kernel particle methods for elastic and plastic problems', in D. J. Benson and R. A. Asaro (eds), *Advanced Computational Methods for Material Modeling*, AMD Vol. 180 and PVP Vol. 268, ASME, New York, 1993, pp. 175–190.
3. W. K. Liu, S. Jun, S. Li, J. Adee and T. Belytschko, 'Reproducing kernel particle methods for structural dynamics', *Int. J. Numer Methods Eng.*, **38**, 1655–1680 (1995).
4. W. K. Liu and C. Oberste-Brandenburg, 'Reproducing kernel and wavelet particle methods', in J. P. Cusumano, C. Pierre and S. T. Wu (eds), *Aerospace Structures: Nonlinear Dynamics and System Response*, AD Vol. 33, ASME, New York, 1993, pp. 39–56.
5. C. K. Chui *An Introduction to Wavelets*, Academic, New York, 1992.
6. Daubechies, *CBMS/NSF Series in Applied Mathematics*, No. 61, *Ten Lectures on Wavelets*, SIAM, Philadelphia, PA, 1992.
7. A. D. Poularikas and S. Seely, *Signals and Systems*, 2nd edn, PWS-Kent, 1987.
8. T. J. R. Hughes, L. Franca and G. M. Hulbert, 'A new finite element formulation for computational fluid dynamics: VIII. The Galerkin/least-square method for advective–diffusion equations', *Comput. Methods Appl. Mech. Eng.*, **73**, 173–189 (1989).
9. F. Shakib and T. J. R. Hughes, 'A new finite element formulation for computational fluid dynamics: IX. Fourier analysis of space–time Galerkin/least-squares algorithms', *Comput Methods Appl. Mech. Eng.*, **87**, 35–58 (1991).
10. C. K. Chui, *Wavelets: A Tutorial in Theory and Applications*, Academic, New York, 1992.